Earth and Planetary Science Letters 491 (2018) 1–10

Contents lists available at ScienceDirect

Earth and Planetary Science Letters

www.elsevier.com/locate/epsl

Reactive transport and mass balance modeling of the Stimson sedimentary formation and altered fracture zones constrain diagenetic conditions at Gale crater, Mars

E.M. Hausrath [a,*], D.W. Ming [b], T.S. Peretyazhko [c], E.B. Rampe [b]

[a] University of Nevada, Las Vegas, United States
[b] NASA Johnson Space Center, United States
[c] Jacobs, NASA Johnson Space Center, United States

ARTICLE INFO

Article history:
Received 9 September 2017
Received in revised form 9 February 2018
Accepted 25 February 2018
Available online xxxx
Editor: W.B. McKinnon

Keywords:
Gale crater
Mars
altered fracture zones
Stimson formation
reactive transport modeling
weathering

ABSTRACT

On a planet as cold and dry as present-day Mars, evidence of multiple aqueous episodes offers an intriguing view into very different past environments. Fluvial, lacustrine, and eolian depositional environments are being investigated by the Mars Science Laboratory *Curiosity* in Gale crater, Mars. Geochemical and mineralogical observations of these sedimentary rocks suggest diagenetic processes affected the sediments. Here, we analyze diagenesis of the Stimson formation eolian parent material, which caused loss of olivine and formation of magnetite. Additional, later alteration in fracture zones resulted in preferential dissolution of pyroxene and precipitation of secondary amorphous silica and Ca sulfate. The ability to compare the unaltered parent material with the reacted material allows constraints to be placed on the characteristics of the altering solutions. In this work we use a combination of a mass balance approach calculating the fraction of a mobile element lost or gained, τ, with fundamental geochemical kinetics and thermodynamics in the reactive transport code CrunchFlow to examine the characteristics of multiple stages of aqueous alteration at Gale crater, Mars. Our model results indicate that early diagenesis of the Stimson sedimentary formation is consistent with leaching of an eolian deposit by a near-neutral solution, and that formation of the altered fracture zones is consistent with a very acidic, high sulfate solution containing Ca, P and Si. These results indicate a range of past aqueous conditions occurring at Gale crater, Mars, with important implications for past martian climate and environments.

1. Introduction

Gale crater, Mars preserves evidence of a variety of both ancient and modern environments. Geochemical, mineralogical, and morphological evidence suggest diagenetic processes occurred after Gale crater formation around 3.7 Ga ago (late Noachian/Early Hesperian) (Grotzinger et al., 2014; Stack et al., 2014; Nachon et al., 2017; Rampe et al., 2017). Ar–K geochronology results from the Sample Analysis at Mars (SAM) instrument indicate that diagenesis could have occurred in Gale crater even after the Hesperian epoch on Mars (<3 Ga; Martin et al., 2017).

These diagenetically altered sediments provide an important window into more recent past aqueous alteration on Mars. However, many questions remain regarding the diagenetic environments and the fluids that generated them. Measurements taken by the Mars Science Laboratory *Curiosity* rover of the sedimentary formations present at Gale crater and the alteration within them can help constrain the composition of these past fluids.

Eolian deposits in Gale crater include modern eolian deposits (active dunes at the Bagnold Dune Field and an inactive eolian bedform characterized at the Gobabeb and Rocknest targets, respectively), as well as the lithified mafic eolian Stimson sandstone formation deposited unconformably on top of and much later than the Murray mudstone (Watkins et al., 2016). The bulk mineralogy of the Stimson formation could be explained by alteration of basaltic eolian deposit-like parent material (i.e., Rocknest and Gobabeb) (Frydenvang et al., 2017; Yen et al., 2017). For instance, the Stimson formation sampled at the Big Sky target most likely formed from a Rocknest eolian deposit-like parent material through reaction with early cementing fluids (Fig. 2A, B; Yen et al., 2017). A further comparison of the diagenetically altered Stim-

* Corresponding author at: Department of Geoscience, 4505 S. Maryland Parkway, Las Vegas, NV 89154-4010, United States.
E-mail address: Elisabeth.Hausrath@unlv.edu (E.M. Hausrath).

https://doi.org/10.1016/j.epsl.2018.02.037
0012-821X/

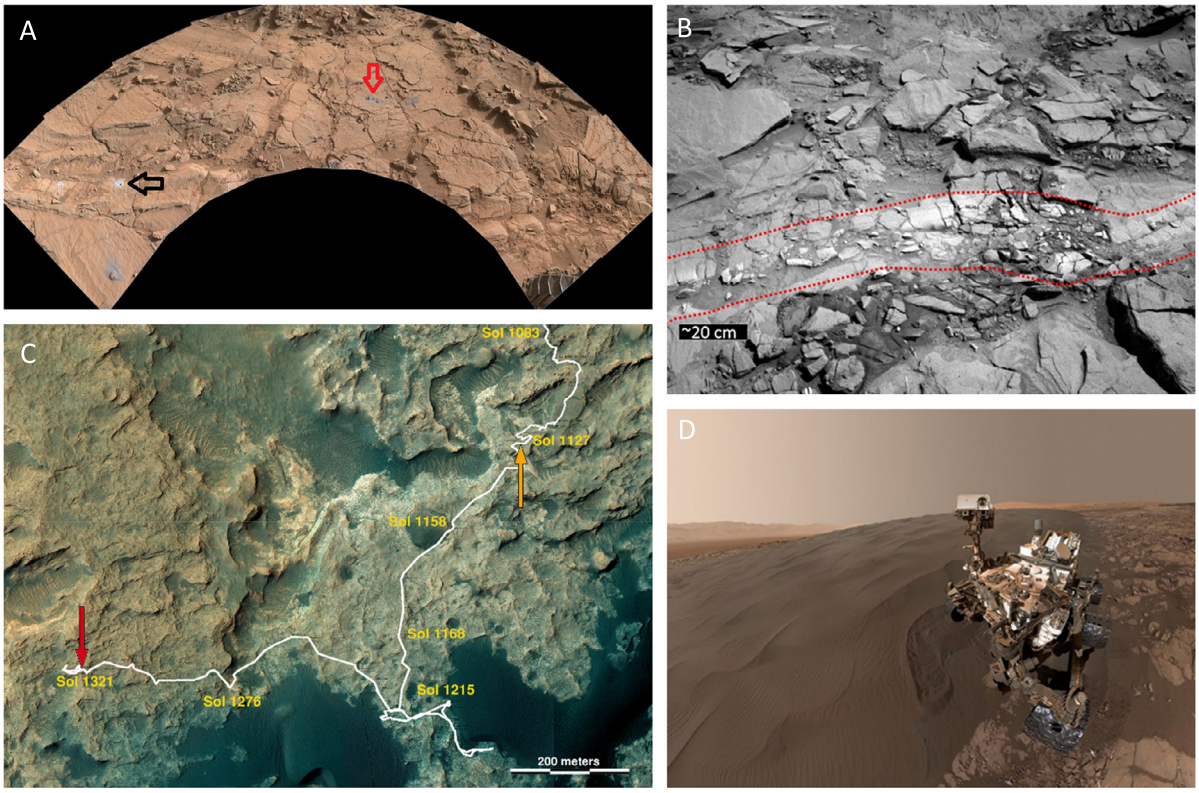

Fig. 1. (A) Image of Big Sky (red arrow) and Greenhorn (black arrow) drill sites, which are outside and inside the altered fracture zone, respectively. For scale, the drillholes are 1.6 cm across. This mosaic was generated from images acquired on Sol 1142. Image credit: NASA/JPL/MSSS. (B) Light-toned altered fracture zone near the Lubango drill site (outlined in red). This image was acquired by the Left Navigation Camera on Sol 1317. Image credit: NASA/JPL-Caltech. (C) Map showing the locations of the Okoruso/Lubango (red arrow) and Big Sky/Greenhorn (orange arrow) drill sites in the Stimson formation sandstone after Yen et al. (2017). The white line indicates the *Curiosity* Rover traverse, with the sols marked in yellow. The map provides an indication of the extent of diagenetic alteration modeled in this paper. Image credit: High Resolution Imaging Science Experiment Camera (HiRISE) in NASA's Mars Reconnaissance Orbiter. NASA/JPL-Caltech/Univ. of Arizona (D) image of the rover on the Bagnold Dunes, sol 1228. Image credit: NASA/JPL-Caltech/MSSS. (For interpretation of the colors in the figure(s), the reader is referred to the web version of this article.)

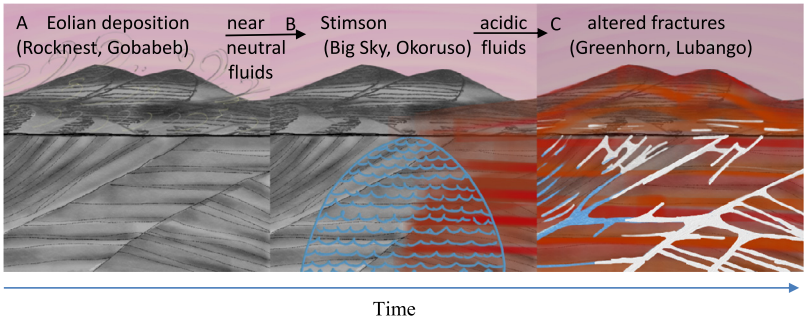

Fig. 2. Conceptual diagram illustrating the scenarios modeled here. Time progresses from left to right – in frame A eolian dunes similar to the modern day Bagnold or Rocknest dunes that will eventually become the modern Stimson formation are deposited on top of the Murray mudstone. In frame B, these dunes are infiltrated with groundwater, which dissolves the olivine and cements the sandstone with iron oxides. The final frame C indicates current conditions; subsequent to the cementation in frame B, fractures in the sandstone are infiltrated with a different solution, resulting in the leached fracture zones observed today.

son formation with the modern dunes (i.e. Gobabeb) can help shed light on early cementing fluids.

In addition, altered fracture zones occur within the lithified Stimson sandstone indicating later alteration fluids that postdate the early cementing fluids moved through the lithified sediments. *Curiosity* investigated two altered fracture zones ~50 cm wide in the Stimson formation (Fig. 1). A pair of samples was drilled from each of the altered fracture zones: Big Sky and Greenhorn, where Big Sky was taken outside of the light-toned fracture and Greenhorn was taken from inside the fracture; and Okoruso and Lubango, where Okoruso was taken from outside of the fracture and Lubango was taken from inside the fracture. Mineralogical and chemical data are available for both of these paired targets, and previous work has examined changes between the bulk Stimson formation and the altered fracture zone sampled as part of the Greenhorn target (Frydenvang et al., 2017; Yen et al., 2017). This work suggests a model of multiple stages of alteration with variable pH and elemental gains and losses (Fig. 2C). Here we test the proposed model of the relationship between the altered fracture zones, the bulk Stimson sedimentary formation, and a putative eolian parent material by quantifying proposed aqueous changes using both mass balance and reactive transport modeling approaches.

We performed geochemical mass balance calculation of τ, the fraction of an element or mineral lost or gained relative to parent material. The calculation of τ allows the identification of geochemical processes that might otherwise be obscured by mobility of multiple elements or changes in volume. Brimhall and Dietrich (1987) and Brimhall et al. (1988) presented the use of τ to ex-

amine the behavior of Ni in laterites and Al in bauxites. Anderson et al. (2002) presented a reformulation of τ applied to weathering in a small steep catchment in the Oregon Coast Range. Mass balance calculations have been used in too many terrestrial studies to cite or review here, as well as in other studies of martian alteration (e.g. Hausrath et al., 2008; McLennan et al., 2014; Adcock and Hausrath, 2015).

Previous reactive transport modeling of terrestrial environments using CrunchFlow has shown that where input mineralogies and aqueous conditions such as pH, transport, duration of aqueous alteration, and solution composition can be constrained, and dissolution rate laws and solubilities are used, reactive transport model outputs correspond well to observed altered material (Maher et al., 2006, 2009; Hausrath et al., 2008; Navarre-Sitchler et al., 2009, 2011; Maher, 2010). The reactive transport code CrunchFlow has been used to successfully interpret weathering on Costa Rica basalts (Hausrath et al., 2008; Navarre-Sitchler et al., 2009, 2011), California soil chronosequences (Maher et al., 2009), ocean floor sediments (Maher et al., 2006), comparing a range of terrestrial settings (Maher, 2010) and Svalbard basalts (Hausrath et al., 2008). Maher et al. (2009) demonstrated that in the well-studied Santa Cruz Soil Chronosequence in California, the presence of clay minerals within the soil could be quantitatively predicted using CrunchFlow and laboratory geochemical input parameters. The history, current state, and potential new research directions of reactive transport models have been recently reviewed (Li et al., 2017) and reactive transport and kinetic–thermodynamic modeling have also been successfully used to interpret weathering on Mars (Zolotov and Mironenko, 2007; Hausrath et al., 2008; McAdam et al., 2008; Hausrath and Olsen, 2013; Adcock and Hausrath, 2015; Gainey et al., in revision). Since the mineralogy and chemical composition of the input parent material and final altered material are known for the Stimson sedimentary formation and altered fracture zones, and mineral dissolution rate laws and solubilities are available in the literature, we can therefore use τ calculations and reactive transport modeling to place constraints on past aqueous conditions at Gale crater.

2. Methods

2.1. Mass balance model

Because mobility of multiple elements can make it difficult to interpret weathered materials, elemental concentrations measured in soils or weathered rocks can be normalized to an assumed immobile element and parent composition to account for this mobility (Brimhall and Dietrich, 1987; Anderson et al., 2002) using the equation below (Eq. (1)):

$$\tau_{i,j} = \frac{C_{j,w}}{C_{j,p}} \frac{C_{i,p}}{C_{i,w}} - 1 \quad (1)$$

Here, $\tau_{i,j}$ is the fraction of mobile element or mineral j lost or gained assuming that element or mineral i is immobile. C is the concentration of the immobile and mobile elements in the parent (p) and weathered (w) materials. Where $\tau_{i,j} > 0$, the element is enriched relative to parent material, where $\tau_{i,j} < 0$, the element is depleted relative to parent material ($\tau_{i,j} = -1$ indicates that the element is completely depleted relative to parent material) and where $\tau_{i,j} = 0$ the element is immobile.

2.1.1. Choice of parent material and immobile element in calculations of τ

The Stimson formation likely formed initially as an eolian deposit (Gupta et al., 2016) which was later altered by diagenetic fluids (Fig. 2). In order to understand diagenesis that occurred in the Stimson formation at Gale crater, Mars, two separate instances of aqueous alteration were studied using mass balance modeling: alteration of an eolian deposit-like parent material such as a modern eolian deposit (Rocknest and Gobabeb) to create the Stimson formation by an early cementing fluid; and formation of the altered fracture zones measured at the Greenhorn and Lubango targets from the Stimson parent material measured in the Big Sky and Okoruso targets, respectively by a later alteration fluid (Fig. 2). These two diagenetic fluids were likely different in their characteristics, and were explored separately in both types of modeling. The use of modern eolian deposits (Rocknest and Gobabeb) as parent material for the Stimson formation follows the approach used on Earth where parent material can be assumed to be similar to recent unweathered sediments if the depositional environment is similar (Chadwick et al., 1990).

The selection of an immobile element for calculations of τ can also be difficult (e.g. Hausrath et al., 2011). We therefore used Alpha Particle X-Ray Spectrometer (APXS) measurements of chemical composition (SOM Table S1) to calculate τ using Si, Al and Ti each as immobile elements (SOM Tables S2 and S3). Titanium is commonly used as an immobile element on Earth, because it often reprecipitates as titanium oxides after it is released from primary silicate minerals. The choice of Al was based on the persistence of plagioclase relative to other mineral phases in measurements from the CheMin X-ray diffractometer on *Curiosity* (see SOM Table S4), and Si was chosen based on the previous suggestions that silica may be passively enriched due to leaching of other elements (Yen et al., 2017). Although all τ values were calculated and examined (SOM Tables 2 and 3), we focus here on Ti as the proposed immobile element due to both observed and modeled dissolution of Si- and Al-containing minerals.

2.2. Reactive transport model

To interpret diagenesis that occurred in the Stimson formation at Gale crater, we performed numerical modeling using the reactive transport code, CrunchFlow (Steefel et al., 2015). CrunchFlow uses a Global Implicit Reactive Transport approach (GIMRT) that simultaneously solves transport and multicomponent reactions (Steefel and Lasaga, 1994; Steefel and MacQuarrie, 1996). Within the model, mineral volumes, surface areas, and porosity are updated after convergence is achieved for each time step. Total surface area is calculated after the shrinking sphere model e.g. Lasaga (1998). Similar to calculations of τ, the two separate instances of aqueous alteration, first the early cementing fluid and then the later alteration fluid (Fig. 2), were explored separately in the reactive transport modeling. We therefore first describe episode-specific model input parameters, followed by the overall model inputs including mineral volumes (Table 1), surface areas, solubilities and rate constants (Table 2), and mineral compositions (Table 3).

2.2.1. Early diagenesis of an eolian deposit-like parent material to create the Stimson formation

To test the hypothesized formation of the Stimson formation from Rocknest and Gobabeb-type eolian deposits, and to determine the characteristics of the early cementing fluid, we conceptualized the alteration as flow occurring through an unconsolidated sediment with porosities of 40% based on eolian terrestrial analogs (Pye and Tsoar, 2008). The model was discretized as 50 cells of 1.6 cm, based on the size of the drill holes and therefore the resolution of those data, with a Dirichlet boundary for aqueous and gaseous species at the surface of the unit, and a flux boundary at the base of the column of cells. The flow rate was set to 1 mm/yr, based conservatively on terrestrial flow rates generated by fluids from compaction (Wilson et al., 2000), and flow occurred form the

Table 1
Mineral volumes (as fractions of the whole rock including porosity) and solution chemistries of initial reacting solutions used in reactive transport modeling.

	Rocknest to Big Sky/Okoruso	Big Sky to Greenhorn	Gobabeb to Big Sky/Okoruso	Okoruso to Lubango
		Mineral volume		
Plagioclase	0.17	0.24	0.15	0.17
Pyroxene	0.12	0.16	0.13	0.14
Glass	0.22	0.13	0.22	0.22
Olivine	0.09	0	0.1	0
Magnetite	0	0.07	0	0.07
Ferrihydrite	1.0×10^{-7}	1.0×10^{-7}	1.0×10^{-7}	1.0×10^{-7}
Porosity	0.4	0.4	0.4	0.4
		Solution chemistry[a] (M)		
SO_4^{2-}		1.5		1.5
PO_4^{3-}		5×10^{-3}		5×10^{-3}
Ca		4×10^{-3}		4×10^{-3}
Si		1×10^{-3}		1×10^{-3}

[a] Where solution chemistries are not reported, a value of 0.5 μM was used for each element present in a mineral in the system. Small amounts of ferrihydrite were added to permit sorption in the model.

top of the column to the base. Models were run until the olivine had dissolved based on observations of no olivine in the Stimson formation targets used in this work (Table 4).

2.2.2. Formation of altered fracture zones from a Stimson-like parent material

In contrast to the diagenesis that generated the Stimson formation as measured at the Big Sky and Okoruso targets, alteration observed near the fractures measured at the Greenhorn and Lubango targets does not appear to be due to uniform fluid flow through the formation, but rather emanating out from the fracture. This alteration was therefore conceptualized in the model as diffusion of the later alteration fluid from the edge of the fracture. The model was discretized as 50 cells of 1.6 cm, based on the size of the drill holes and therefore the resolution of those data, with a Dirichlet boundary for aqueous and gaseous species at the fracture surface, and a flux boundary at the end of the column of cells. Tortuosity, which controls the diffusive flux, was set to 0.5 based on values for an Fe-oxide cemented terrestrial sandstone formed in an arid environment (Laudone et al., 2015).

2.2.3. Mineral surface areas

In order to estimate mineral surface areas for our modeling work, we calculated surface roughnesses for relevant minerals from the Rocknest eolian deposit and the Gobabeb target in the Bagnold dune field, including plagioclase, pyroxene, olivine, magnetite and glass as described in the SOM Supplementary Methods. Surface areas for the secondary minerals gypsum, amorphous silica, jarosite, amorphous Fe phosphate and iron oxides including ferrihydrite and magnetite were based on literature values as described in the SOM Supplementary Methods. To model surface sorption, surface sites were assumed to be 1.78×10^{-5} mol sites m^{-2} $Fe(OH)_3$ (Arora et al., 2015), and complexation constants are reported in the SOM Methods.

Mineral volumes (as fractions) were input for phases measured by CheMin in the Rocknest and Gobabeb targets (plagioclase, pyroxene, glass and olivine) for modeling alteration by an early cementing fluid and Okoruso and Big Sky targets (plagioclase, pyroxene, glass, and magnetite) (Table 1) for modeling alteration by later alteration fluids. Only phases measured at greater than 5% by CheMin were included to simplify modeling, with the mineral volume then decreased to account for the porosity described above. These mineral fractions are used in the initial reaction of the minerals with solution, and then are allowed to evolve within the model. The secondary minerals gypsum, amorphous silica, jarosite, amorphous Fe phosphate and iron oxides including ferrihydrite and magnetite were also allowed to precipitate and dissolve in the model even if not initially present (hematite was not included because, as it is more crystalline, it would be more likely to form from a less crystalline precursor such as ferrihydrite).

The dominant Ca sulfate mineral measured in Greenhorn by CheMin is anhydrite with small amounts of bassanite and no gypsum, and Okoruso contains a mixture of anhydrite and bassanite (Table 4). Anhydrite is generally considered to form at higher temperatures than gypsum (Freyer and Voigt, 2003), although previous work has shown that anhydrite can also precipitate at low temperatures from very high salinity brines (Dixon et al., 2015). Gypsum has also been shown to dehydrate to bassanite and anhydrite under Mars atmospheric conditions (Vaniman et al., 2017). We therefore include gypsum in the model, although whether it is gypsum or anhydrite that originally formed on Mars is underconstrained.

Mineral compositions, solubilities and rate constants were used from the literature as shown in Tables 2 and 3. In each model, atmospheric CO_2 and O_2 concentrations were set to current martian atmospheric concentrations, and temperature was set to 1 °C to represent low temperature conditions consistent with current Mars, as well as the mineralogical observations of Gale crater. Evidence for dissolution of olivine rather than serpentinization (Yen et al., 2017) suggests temperatures below ~85 °C (Barnes and O'Neil, 1978), and opal-A (Yen et al., 2017) would suggest temperatures below ~35–50 °C (Mackenzie, 2005). These estimates are reasonably consistent with modeling by Borlina et al. (2015), which indicated temperature maxima of 30–80 °C (Scenario 2) and 75–125 °C (Scenario 1), and which also reported that the presence of smectite in Yellowknife is consistent with little diagenesis possibly due to lower temperatures. Future work should include a test of the effect of temperature.

2.2.4. Aqueous conditions tested

The aqueous conditions represent fundamentally the question we are addressing in this work – what are the characteristics of the early cementing and later alteration fluids that once flowed through Gale crater? We therefore varied pH from 2–9 in the reacting solutions based on acidic conditions inferred from the presence of jarosite in some samples from the Murray formation in Gale crater (Rampe et al., 2017), and pH measurements of martian soils made at the Phoenix landing site (Kounaves et al., 2010). The balancing cation was set to Na^+ and the balancing anion to Cl^-, and a range of both dilute solutions and solutions enriched in S, Ca, Si and P were tested as the initial solution compositions within the model (solution compositions evolve with reaction within the model), with solution compositions for reported results shown in Table 1. Oxidation state was not varied in model inputs, but evolved within the model with reaction similarly to other geochemical parameters.

Table 2
Dissolution and precipitation rate constants, activation energies, surface areas and equilibrium constants for reactive transport modeling.

Mineral	$\log k_{H^+diss}$ (mol m^{-2} s^{-1})	n_{H^+}	Ae (kcal mol^{-1}) (acidic)	$\log k_{OH^-diss}$ (mol m^{-2} s^{-1})	n_{OH^-}	Ae (kcal mol^{-1}) (basic)	$\log k_{neutral}$	Ae (kcal mol^{-1}) (neutral)	$\log k_{ppn}$	Ae (kcal mol^{-1}) (ppn)	surface area* ($m^2 g^{-1}$)	log K (25 °C)
Plagioclase	−8.88[b]	0.541[b]	12.79[b]	−9.5[f]	0.4[f]	12.79[b]	−11.47[b]	13.72[b]			0.157[r]	13.88[j]
Pyroxene	−6.82[b]	0.7[b]	18.64[b]								0.238[r]	9.08[k]
Glass	−6.188[c]	1.07[c]	12.19[c]	−10.323[c]	0.1656[c]	12.19[c]					0.236[s]	17.25[p]
Olivine	−5.88[d]	0.47[d]	19.29[d]								0.133[r]	23.78[j]
Amorphous silica							−12.77[g]	16.42[g]	−9.42[g]	11.90[g]	2.387[t]	−2.7136[q]
Gypsum							−6[h]	0[b]			0.19[u]	−4.4823[h]
Ferrihydrite	−10.98[e]	0.43[e]	20.67[b]								23.49[v]	5.6556[q]
Magnetite	−8.59[b]	0.279[b]	4.45[b]				−10.78[b]	4.45[b]			0.22[w]	10.4724[q]
Jarosite	−6.487[a]	0.899[a]	18.89[a]	−10.964[a]	0.392[a]	18.89[a]					0.22[a]	−9.3706[q]
Amorphous Fe-phosphate	−13.03[y]	1.38[y]	9.56[z]								12.19[y]	−24[x]

* Surface area in contact with weathering fluids, 10% of the calculated or measured surface area (Velbel, 1993). a–z refer to sources provided in Table S5 in the SOM.

3. Results and discussion

3.1. Early diagenesis of an eolian deposit-like parent material to create the Stimson formation

CheMin measurements of the powdered <150 μm fraction from the drill hole at Big Sky from the bulk Stimson formation and samples from the Rocknest eolian deposit have been previously shown to be strikingly similar (Yen et al., 2017 and see SOM Table S4). The main difference between the Big Sky and Rocknest measurements is the presence of olivine in the Rocknest eolian deposit, which is absent in the Big Sky target, and the presence of far more abundant Fe oxides, particularly magnetite, in the Big Sky target. Similarly, the Bagnold Dunes mineralogy measured from the Gobabeb sample is comparable to that measured at Rocknest, and, like Big Sky, the Okoruso sample of the bulk Stimson formation differs from Rocknest and Gobabeb measurements largely by the absence of olivine and larger quantities of magnetite (SOM Table S4). Here the dissolution of olivine and precipitation of Fe oxides provides constraints on the early cementing fluid generating the Stimson formation from a putative mafic eolian parent material.

Models run with both the Gobabeb and Rocknest eolian deposit-like parent material in solutions with pH values of 6–8 show significant precipitation of magnetite, whereas under more acidic and alkaline conditions minimal magnetite precipitates (Fig. 3; Table 4; SOM). These results are consistent with the much greater mobility of ferric Fe under strongly acidic and alkaline conditions. Under pH values of 6–8, olivine also dissolves and the other primary minerals persist, consistent with observations by CheMin (Fig. 3).

We also examine our mass balance modelling comparing the Stimson formation to putative eolian parent material by calculating the fraction of a mobile element lost or gained, τ. We focus our discussion here on Gobabeb as the parent material for Big Sky and Okoruso due to the variability in Ti between soil target Portage, scuffed and unscuffed samples in the Rocknest eolian deposit (Table S1), and we focus on Ti as the proposed immobile element due to dissolution of Si- and Al-containing minerals. The τ values calculated for alteration of Gobabeb to Big Sky indicate that Na, Mg, Al, Si, P, K, Ca, Mn, Fe, and Ni are slightly to moderately depleted; S, Cl Zn, and Br are enriched; and little change is observed in Cr. Similarly, τ values calculated for alteration of Gobabeb to Okoruso indicate that Mg, Al, Si, P, S, K, Ca, Cr, Mn, Fe, and Ni are depleted, and Na, Cl, Zn, and Br are enriched. These results are consistent with diagenesis consisting primarily of leaching (no major rock-forming elements are enriched) by solutions that may also be enriched in the anions common on Mars (sulfate and chloride; enrichment in sulfate is observed for Big Sky but not Okoruso). Previous work has also argued that enrichments in Ni, Br, Zn, and Cl may occur in Fe-rich cements in other rocks at Gale crater (Schmidt et al., 2013; McLennan et al., 2014). The fraction of an element lost or gained during weathering in our reactive transport modeling was also compared to calculated τ values, and pH = 6 is quite comparable (Table 5). These modeling results therefore indicate that early diagenesis of the Stimson formation is consistent with aqueous alteration under near-neutral pH conditions.

3.2. Formation of the altered fracture zones from the bulk Stimson formation

The presence of the fracture zones represented by the Greenhorn and Lubango targets and the unaltered material near them measured as part of the Big Sky and Okoruso targets, respectively, allows a quantification of the chemistry of the late alteration fluid (Yen et al., 2017). Chemical and mineralogical changes indicate

Table 3
Mineral stoichiometry used in modeling.

Mineral	Mineral formula
Plagioclase	$Na_{0.55}Ca_{0.45}Al_{1.45}Si_{2.55}O_8 + 5.8H^+ = 0.55Na^+ + 0.45Ca^{2+} + 1.45Al^{3+} + 2.55SiO_2(aq) + 2.9H_2O$
Pyroxene	$Mg_{0.38}Fe_{0.62}SiO_3 + 2H^+ = 0.38Mg^{2+} + 0.62Fe^{2+} + SiO_2(aq) + H_2O$
Glass	$SiAl_{0.29}O_2(OH)_{0.86} + 0.86H^+ + 1.14H_2O = H_4SiO_4 + 0.29Al^{3+}$
Olivine	$Mg_{1.04}Fe_{0.96}SiO_4 + 4H^+ = 1.04Mg^{2+} + 0.96Fe^{2+} + SiO_2(aq) + 2H_2O$
Amorphous silica	$SiO_2(am) = SiO_2(aq)$
Gypsum	$CaSO_4.2H_2O = Ca^{2+} + SO_4^{2-} + 2H_2O$
Ferrihydrite	$Fe(OH)_3 + 3H^+ = Fe^{3+}(aq) + 3H_2O$
Magnetite	$Fe_3O_4 + 8H^+ = Fe^{2+} + 2Fe^{3+} + 4H_2O$
Jarosite	$KFe_3(SO_4)_2(OH)_6 + 6H^+ = K^+ + 3Fe^{3+} + 2SO_4^{2-}$
Am Fe–PO_4	$FePO_4.xH_2O + H^+ = Fe(OH)_2^+ + H_2PO_4^- + (x-1)H_2O$

Plagioclase compositions were chosen based on plagioclase compositions for Big Sky and Okoruso reported by Yen et al. (2017). Since descriptions of pyroxene included pigeonite and orthopyroxene (Yen et al., 2017), the pyroxene composition was simplified to a Mg–Fe-containing pyroxene, and the dissolution rate law for augite used. The glass was based on a terrestrial dacitic glass (Wolff-Boenisch et al., 2004) based on descriptions by Yen et al. (2017), and the olivine composition was based on the description of forsterite in CheMin data. The number of waters included in the amorphous iron phosphate was chosen to be two to be similar to strengite. Solutions generated in the modeled alteration were also tested against the sulfate phases epsomite and kieserite, and were below saturation, but because mineral dissolution rates for these phases were insufficiently constrained, we do not include them here.

Table 4
A comparison of measured mineral volumes versus model outputs (model mineral inputs are given in Table 1). Modeled mineral volumes are adjusted to 0% pore space to be more comparable to the CheMin measured mineral volumes.

Mineral	Big Sky measured		Okoruso measured		Gobabeb modeled	Greenhorn measured		Modeled	Lubango measured		Modeled
	%	Error	%	Error	%	%	Error	%	%	Error	%
Plagioclase	36.5	1.8	27.2	1.7	26.2/26.3	14.7	0.8	14.4/24.5	11.7	0.6	9.7/16.9
K_feldspar	1.1	0.6	1.9	0.7							
Olivine											
Augite											
Pigeonite	17	1.4	13.5	1.3		1.6	0.5		1.6	0.4	
Orthopyroxene	8.4	1.8	7.2	1.4	23.0	2.7	0.7	0.3/11.8	2.8	0.5	0.1/8.63
Magnetite	10.3	0.6	11.2	0.7	6.0/6.2	6.1	0.3	0.8/15.8	3	0.2	0/16.21
Hematite	3	0.5	0.7	0.4		2.1	0.3		0.6	0.2	
Ilmenite											
Gypsum								5.3/10.4	0.6	0.2	4.06/8.75
Bassanite			0.8	0.4		1.4	0.3		2.4	0.3	
Anhydrite	1.2	0.3	0.5	0.4		5.6	0.3		3.3	0.2	
Quartz	1.4	0.3	0.9	0.3		0.8	0.2		0.9	0.2	
Fluorapatite	1.1	0.5	1	0.4							
Amorphous	20	10	35	15	44.6/44.8	65	20	42.7/74.2	73	20	54.2/81.4

Depth values are given for 6.4–8.0 cm and pH = 6 for Bagnold, and for 1.6–3.2 cm and pH = 3 for Big Sky and Lubango.

Table 5
The fraction of a mobile element lost or gained, τ calculated using assumed immobile element Ti and using the chemical composition of Big Sky and Okoruso as parent material for Greenhorn and Lubango, respectively, and Gobabeb as parent material for Big Sky and Okoruso.

Oxide	Parent = Gobabeb			Parent = Big Sky		Parent = Okoruso	
	$\tau_{Ti,j}$ Big Sky	$\tau_{Ti,j}$ Okoruso	Modeled*	$\tau_{Ti,j}$ Greenhorn	Modeled*	$\tau_{Ti,j}$ Lubango	Modeled*
Na_2O	−0.02	0.08	−0.17	−0.15	−0.35/−0.56	−0.52	−0.37/−0.59
MgO	−0.25	−0.14	−0.66	−0.82	−0.53/−0.99	−0.91	−0.61/−0.99
Al_2O_3	−0.14	−0.12	−0.11	−0.68	−0.28/−0.49	−0.8	−0.23/−0.49
SiO_2	−0.22	−0.20	−0.22	0.42	0.004/0.39	0.26	0.003/0.39
P_2O_5	−0.04	−0.13	NIM	0.89	NIM	0.7	NIM
SO_3	0.69	−0.81	NIM	1.33	NIM	19.58	NIM
Cl	1.01	0.09	NIM	−0.52	NIM	−0.56	NIM
K_2O	−0.16	−0.35	NIM	−0.29	NIM	−0.22	NIM
CaO	−0.25	−0.22	−0.17	0.18	0.07/0.39	0.16	0.09/0.53
TiO_2	0.00	0.00	NIM	0	NIM	0	NIM
Cr_2O_3	0.00	−0.09	NIM	−0.3	NIM	−0.21	NIM
MnO	−0.29	−0.11	NIM	−0.94	NIM	−0.87	NIM
FeO	−0.20	−0.03	−0.12/−0.14	−0.41	0.05/−0.95	−0.83	0.07/−1.00
Ni	−0.37	−0.33	NIM	−0.56	NIM	−0.92	NIM
Zn	0.37	0.54	NIM	−0.67	NIM	−0.79	NIM
Br	3.89	1.94	NIM	0.96	NIM	−0.48	NIM

NIM = Not included in Input Minerals in modeling.
Elemental compositions for Gobabeb, Rocknest, Big Sky, and Okoruso were used from the Planetary Data Systems (PDS: https://pds.nasa.gov/) and are given in the SOM (Table S1). The chemical composition used as parent for Rocknest and Gobabeb are the average of the values in the PDS.

* Because Ti minerals were not explicitly included in the model inputs, the fraction lost from the model results is calculated as $\frac{C_{j,w}}{C_{j,p}} - 1$. Depth values are given for 6.4–8.0 cm and pH = 6 for Bagnold, and for 1.6–3.2 cm and pH = 3 for Big Sky and Lubango.

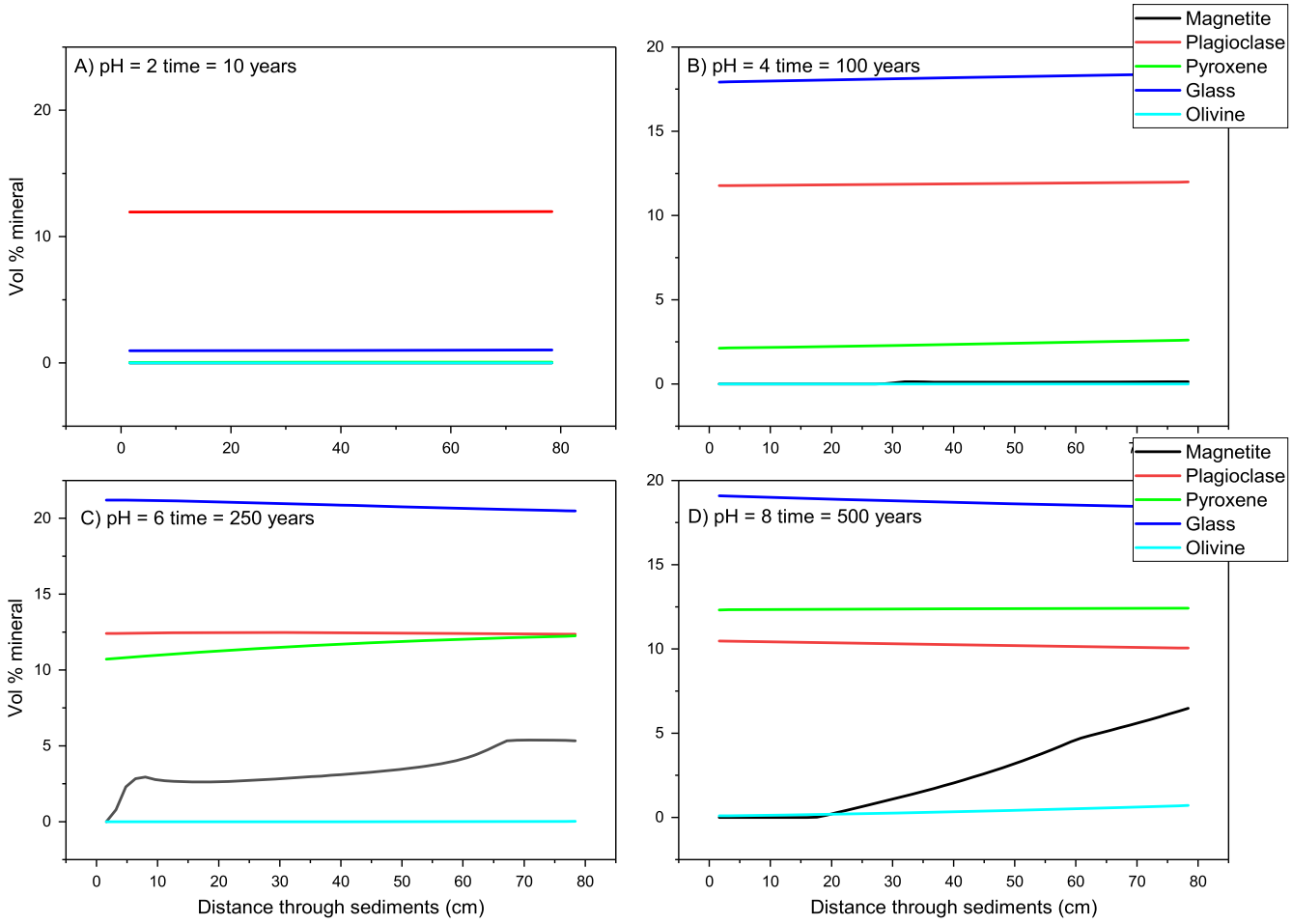

Fig. 3. Model outputs of a Gobabeb eolian deposit-like parent material (15% plagioclase, 13% pyroxene, 22% dacitic glass, and 10% olivine – see also Table 1) altered at A) pH = 2, B) pH = 4, C) pH = 6 and D) pH = 8 with flow occurring from left to right. Results at higher pH result in the absence of olivine, the preservation of other primary minerals, and the formation of magnetite, consistent with CheMin measurements of the Big Sky target (see also Table 4 and SOM). These results suggest that early diagenesis in the Stimson formation is consistent with this type of near-neutral aqueous alteration. Mineral phases present at less than 0.1% (ferrihydrite, amorphous silica and $Fe(PO_4)$ am) are not shown.

the loss of plagioclase, magnetite and pyroxene, and the increase primarily of amorphous silica (opal A) and calcium sulfate (SOM Table S4). To determine which model conditions were most consistent with observations, we compared model outputs of plagioclase and pyroxene, the fraction of elements lost or gained, the secondary minerals formed, and the width of the zone of alteration.

Dissolution of plagioclase and pyroxene within the models is most consistent with CheMin observations when the late alteration fluid was very acidic, with the best correlation occurring at pH = 3 (Table 4; Fig. 4 and SOM). Magnetite also dissolves within the models under acidic conditions, which is consistent with the observation of decreased magnetite in Greenhorn and Lubango relative to Big Sky and Okoruso. Amorphous silica precipitated in the models with or without additional silica in solution – small amounts of silica in solution (1 mM, similar to concentrations generated in Mars analog experiments by interaction of acidic solutions with mafic minerals; Hausrath and Brantley, 2010) contributed to larger enrichments in silica more comparable to τ values calculated for formation of Greenhorn and Lubango (Table 5). When abundant sulfate, consistent perhaps with solutions interacting with sulfide bodies proposed by Yen et al. (2017), and Ca were present in the reacting solution, gypsum also precipitated.

We also examine the results of our mass balance modeling comparing the changes in elemental chemistry of Greenhorn relative to Big Sky and Lubango relative to Okoruso using τ. When examining τ values calculated for elemental changes from Okoruso to Lubango and Big Sky to Greenhorn with the assumed immobile element Ti, all elements are depleted in both cases except for Si, P, S, and Ca, which are enriched for both cases, and Br is enriched in the formation of Greenhorn from Big Sky. Our reactive transport modeling also requires the addition of S, Si, P and Ca to the reacting solutions for model outputs to match observations from Mars. Although only trace amounts of amorphous Fe-phosphate precipitated in our models (SOM), phosphate sorbed to the Fe oxy-hydroxide surfaces in comparable amounts in moles/g sediment to measurements by APXS (SOM). As expected, modeled phosphate sorption increased with decreasing pH (SOM), and trends in the fraction of an element lost or gained in the model under acidic conditions corresponded reasonably well with τ values calculated for APXS observations (Table 5). We therefore conclude that the model conditions that are most consistent with observations of altered fracture zones at Gale crater are low pH, with abundant sulfate, and Ca, Si and phosphate present in solution.

Gypsum precipitated in the models only when very high concentrations of sulfate and enrichments of Ca were present. Although mineral precipitation kinetics remain an area of active research, and the relationship between mineral precipitation and saturation state is more complicated than the traditional models by which it is usually represented (Bracco et al., 2014), these results do indicate that solutions precipitating gypsum on Mars are likely very high in sulfate and enriched in Ca. The very high

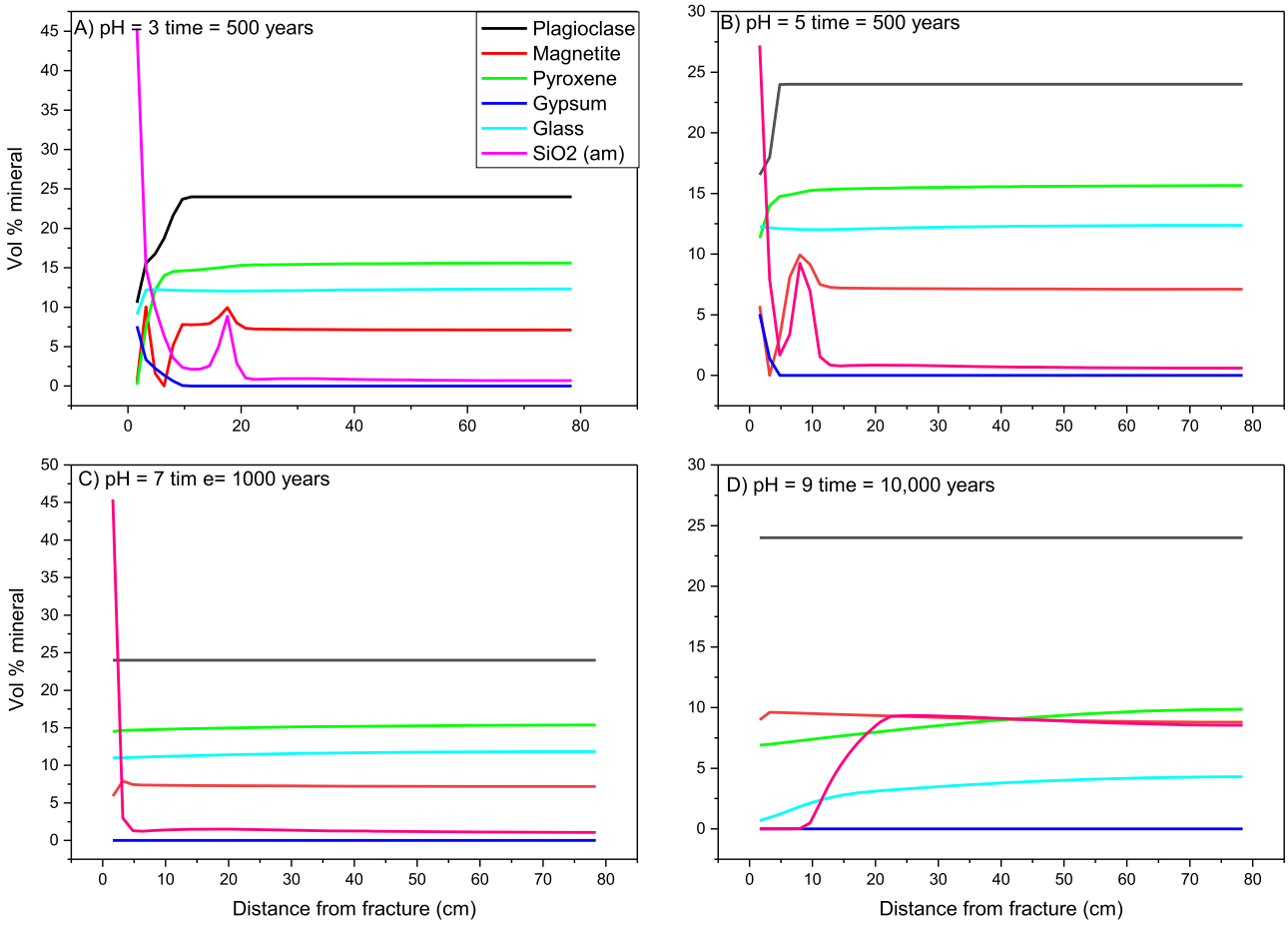

Fig. 4. Model outputs of a Big Sky target parent material (24% plagioclase, 16% pyroxene, 13% glass, and 7% magnetite) altered under A) pH = 3, B) pH = 5, C) pH = 7 and D) pH = 9 conditions with diffusion occurring from the fracture. Results under very acidic conditions (pH = 3) result in dissolution and precipitation comparable to CheMin measurements of the Greenhorn target. See also Tables 4 and 5 and SOM for further comparisons of the different pH conditions. Mineral phases present at less than 0.1% (ferrihydrite, jarosite and $Fe(PO_4)$ am) are not shown.

sulfate content is consistent with fluids predicted by Yen et al. (2017) from solution interaction with sulfide bodies, and aqueous Ca might result from leaching Ca-rich phases such as plagioclase and Ca-sulfates. Similar leaching and transport of the dissolution products of quickly dissolving calcium phosphate phases (Adcock et al., 2013) might also explain the observed enrichments in phosphate (Table 5). Our modeling generates mineral dissolution and silica enrichments without the presence of the alkaline solutions proposed by Yen et al. (2017). However, our models did not include as a constraint the less than 1% carbonate detected by SAM (Sutter et al., 2017). Carbonate dissolves very rapidly under acidic conditions, and the presence of carbonate and alkaline soil conditions have been previously documented at the Phoenix landing site (Kounaves et al., 2010). Our modeling results do not preclude such additional later alkaline solutions, which may indeed be likely based on observations from the Phoenix landing site, and are in agreement with mass balance work by Yen et al. (2017) that alteration fluids likely contained at least small amounts of silica in solution.

3.3. *Modeling results in the context of the aqueous history of Gale crater*

Previous work has examined diagenetic fluids in both the Stimson sedimentary formation (Yen et al., 2017), as well as the Murray mudstones (Hurowitz et al., 2017; Rampe et al., 2017). Here we compare our modeling results to different proposed aqueous scenarios in Gale crater, to help shed light on the overall diagenetic history of the region.

Rampe et al. (2017) postulate diagenesis of the Murray formation by pore fluids that were at least locally mildly to moderately acidic based on the presence of jarosite. These environments were not extremely acidic or long-lived, thus preserving minerals susceptible to dissolution such as fluorapatite (Rampe et al., 2017). Alternatively, sediment deposition within the Murray formation could occur in near-neutral redox stratified lake waters, with localized acidic fluids of pH 2–4 due to oxidation of Fe(II) sulfide grains resulting in jarosite formation (Hurowitz et al., 2017). This scenario also explains secondary minerals formed within the Murray formation and consistent with CheMin observations (Rampe et al., 2017). The proposed scenarios predict that diagenesis by both neutral and acidic solutions of variable redox state were required to form the observed mineralogy of the Murray formation (Hurowitz et al., 2017; Rampe et al., 2017). Although the Stimson formation unconformably overlies and postdates the Murray mudstone (Watkins et al., 2016; Frydenvang et al., 2017), similar fluids might have moved through both of them. Gale crater is the lowest point for a thousand kilometers in any direction (Grotzinger et al., 2015) leading to groundwater flow into the crater (Hurowitz et al., 2017). As a result, diagenesis occurring in both formations was likely similar and controlled by the groundwater pH and redox state. Observations of alteration zones in the Murray formation further support the hypothesis of similar diagenesis in both formations. Yen et al. (2017) noted that alteration zones measured in the Murray mudstone (Cody target) compared to the nearby unaltered Murray mudstone (Ferdig target) showed similar trends to those modeled here in the Stimson formation.

Our modeling results showed that the observed changes due to diagenesis in the Stimson formation could be explained by solution pH. In contrast to the lake model proposed by Hurowitz et al. (2017), redox changes were not required to obtain the observed mineralogy. However, future large scale modeling should also examine variation in oxidation state as a diagenetic factor. Reactive transport modelling showed that diagenesis in near-neutral early cementing solutions followed by highly acidic, saline late alteration solutions (Fig. 2) resulted in secondary minerals and alteration zones that are presently observed in the Stimson formation. Early cementing solutions are likely to have been more alkaline due to the expected interaction with mafic minerals. Later alteration solutions may have been more acidic due to oxidation of Fe(II) sulfides, dissolution of Fe(III) sulfates, or interactions between magmatic volatiles and groundwater (Hurowitz et al., 2017; Rampe et al., 2017). Decreases in water:rock ratio would likely have enhanced such acidifying mechanisms. Most importantly, our results help shed light on the water that persisted long after the lakes were present in Gale crater (Grotzinger et al., 2014), examining the extended presence of aqueous environments in this region of Mars.

4. Conclusions

A combination of geochemical mass balance modeling with reactive transport modeling allows quantitative constraints to be placed on diagenetic scenarios and past aqueous environments in Gale crater, Mars. Our results show that at least two separate diagenetic events are required for development of the present day Stimson formation. Interaction of an eolian parent material, such as the Gobabeb- or Rocknest-like eolian deposits, with near-neutral cementing fluids led to dissolution of olivine and precipitation of Fe oxides. Such diagenetic processes resulted in the mineralogy and geochemistry observed in the bulk Stimson formation measured in Big Sky and Okoruso. In the second event, interaction of the bulk Stimson formation with a later very acidic fluid, containing Ca, P and Si and highly enriched in S, led to formation of the altered fracture zones measured in the Greenhorn and Lubango targets. These results, which test specific scenarios using quantitative modeling, are largely in agreement with the proposed diagenetic scenarios based on direct observations e.g. Hurowitz et al. (2017), Rampe et al. (2017), Yen et al. (2017).

The main result of this work is quantitative constraints on the aqueous environments that extended long after the lakes existed in Gale crater (Grotzinger et al., 2014; Hurowitz et al., 2017). The deposition and diagenesis of the Murray formation likely took place in the Hesperian epoch between 3.8 and 3.1 Ga (Grotzinger et al., 2015; Hurowitz et al., 2017). Although the exact time of deposition of the Stimson formation is unknown, its formation and diagenesis happened much later than the Murray mudstone, possibly extending into the Amazonian epoch (<3 Ga) (Frydenvang et al., 2017). These results therefore help constrain recent and diverse aquatic environments in Gale crater.

Author contributions

E.M.H. and D.W.M. conceived the project, and E.M.H. performed the mass balance and reactive transport modeling and wrote the first draft of the manuscript. All authors contributed to interpretation of the data and writing of the manuscript.

Acknowledgements

We acknowledge funding from the NASA Mars Data Analysis Program Grant 80NSSC17K0581. We would like to thank Carl Steefel for providing the code CrunchFlow, and Peter Sbraccia, Arlaine Sanchez and Chris Adcock for helpful assistance. We also appreciate thoughtful comments from EPSL Editor William McKinnon, and reviewers Kirsten Siebach and Benjamin Tutolo that greatly improved the paper.

Appendix A. Supplementary material

Supplementary material related to this article can be found online at https://doi.org/10.1016/j.epsl.2018.02.037.

References

Adcock, C., Hausrath, E., Forster, P., 2013. Readily available phosphate from minerals in early aqueous environments on Mars. Nat. Geosci. 6, 824–827.

Adcock, C.T., Hausrath, E.M., 2015. Weathering profiles in high-P rocks at Gusev Crater, Mars, suggest dissolution of phosphate minerals into near-neutral waters. Astrobiology 15, 1060–1075.

Anderson, S.P., Dietrich, W.E., Brimhall, G.H., 2002. Weathering profiles, mass balance analysis, and rates of solute loss: linkages between weathering and erosion in a small, steep catchment. Geol. Soc. Am. Bull. 114 (9), 1143–1158.

Arora, B., Şengör, S.S., Spycher, N.F., Steefel, C.I., 2015. A reactive transport benchmark on heavy metal cycling in lake sediments. Comput. Geosci. 19, 613–633.

Barnes, I., O'Neil, J.R., 1978. Present day serpentinization in New Caledonia, Oman and Yugoslavia. Geochim. Cosmochim. Acta 42, 144–145.

Borlina, C.S., Ehlmann, B.L., Kite, E.S., 2015. Modeling the thermal and physical evolution of Mount Sharp's sedimentary rocks, Gale crater, Mars: implications for diagenesis on the MSL Curiosity rover traverse. J. Geophys. Res., Planets 120, 1396–1414.

Bracco, J.N., Stack, A.G., Higgins, S.R., 2014. Magnesite step growth rates as a function of the aqueous magnesium: carbonate ratio. Cryst. Growth Des. 14, 6033–6040.

Brimhall, G., Dietrich, W.E., 1987. Constitutive mass balance relations between chemical composition, volume, density, porosity, and strain in metasomatic hydrochemical systems: results on weathering and pedogenesis. Geochim. Cosmochim. Acta 51, 567–587.

Brimhall, G.H., Lewis, C.J., Ague, J.J., Dietrich, W.E., Hampel, J., Teague, T., Rix, P., 1988. Metal enrichment in bauxites by deposition of chemically mature aeolian dust. Nature 333, 819–824.

Chadwick, O.A., Brimhall, G.H., Hendricks, D.M., 1990. From black box to a grey box: a mass balance interpretation of pedogenesis. Geomorphology 3, 369–390.

Dixon, E.M., Elwood Madden, A.S., Hausrath, E.M., Elwood Madden, M.E., 2015. Assessing hydrodynamic effects on jarosite dissolution rates, reaction products, and preservation on Mars. J. Geophys. Res., Planets 120, 625–642.

Freyer, D., Voigt, W., 2003. Crystallization and phase stability of $CaSO_4$ and $CaSO_4$-based salts. Monatsh. Chem. 134, 693–719.

Frydenvang, J., Gasda, P.J., Hurowitz, J.A., Grotzinger, J.P., Wiens, R.C., Newsom, H.E., Edgett, K.S., Watkins, J., Bridges, J.C., Maurice, S., Fisk, M.R., Johnson, J.R., Rapin, W., Stein, N.T., Clegg, S.M., Schwenzer, S.P., Bedford, C.C., Edwards, P., Mangold, N., Cousin, A., Anderson, R.B., Payré, V., Vaniman, D., Blake, D.F., Lanza, N.L., Gupta, S., Van Beek, J., Sautter, V., Meslin, P.Y., Rice, M., Milliken, R., Gellert, R., Thompson, L., Clark, B.C., Sumner, D.Y., Fraeman, A.A., Kinch, K.M., Madsen, M.B., Mitrofanov, I.G., Jun, I., Calef, F., Vasavada, A.R., 2017. Diagenetic silica enrichment and late-stage groundwater activity in Gale crater, Mars. Geophys. Res. Lett. 44 (10), 4716–4724.

Gainey, S.R., Hausrath, E.M., Hurowitz, J.A., in revision. Thermodynamic and kinetic assessment of Al-capped Clay Mineral Profiles at Mawrth Vallis, Mars. J. Geophys. Res., Planets.

Grotzinger, J.P., Gupta, S., Malin, M.C., Rubin, D.M., Schieber, J., Siebach, K., Sumner, D.Y., Stack, K.M., Vasavada, A.R., Arvidson, R.E., Calef, F., Edgar, L., Fischer, W.F., Grant, J.A., Griffes, J., Kah, L.C., Lamb, M.P., Lewis, K.W., Mangold, N., Minitti, M.E., Palucis, M., Rice, M., Williams, R.M.E., Yingst, R.A., Blake, D., Blaney, D., Conrad, P., Crisp, J., Dietrich, W.E., Dromart, G., Edgett, K.S., Ewing, R.C., Gellert, R., Hurowitz, J.A., Kocurek, G., Mahaffy, P., McBride, M.J., McLennan, S.M., Mischna, M., Ming, D., Milliken, R., Newsom, H., Oehler, D., Parker, T.J., Vaniman, D., Wiens, R.C., Wilson, S.A., 2015. Deposition, exhumation, and paleoclimate of an ancient lake deposit, Gale crater, Mars. Science 350.

Grotzinger, J.P., Sumner, D., Kah, L., Stack, K., Gupta, S., Edgar, L., Rubin, D., Lewis, K., Schieber, J., Mangold, N., 2014. A habitable fluvio-lacustrine environment at Yellowknife Bay, Gale crater, Mars. Science 343, 1242777.

Gupta, S., Banham, S., Rubin, D., Watkins, J., Sumner, D., Grotzinger, J.P., Lewis, K., Edgett, K.S., Edgar, L., Stack, K., Day, M., Ewing, R., Lapotre, M., 2016. Anatomy of an ancient aeolian sandstone on Mars: the Stimson formation, Gale crater, Mars. In: Division for Planetary Sciences Meeting Abstracts, p. 48.

Hausrath, E., Navarre-Sitchler, A., Sak, P., Williams, J., Brantley, S., 2011. Soil profiles as indicators of mineral weathering rates and organic interactions for a Pennsylvania diabase. Chem. Geol. 290, 89–100.

Hausrath, E.M., Brantley, S.L., 2010. Basalt and olivine dissolution under cold, salty, and acidic conditions: what can we learn about recent aqueous weathering on Mars? J. Geophys. Res., Planets 115.

Hausrath, E.M., Navarre-Sitchler, A.K., Sak, P.B., Steefel, C.I., Brantley, S.L., 2008. Basalt weathering rates on Earth and the duration of liquid water on the plains of Gusev Crater, Mars. Geology 36, 67–70.

Hausrath, E.M., Olsen, A.A., 2013. Using the chemical composition of carbonate rocks on Mars as a record of secondary interaction with liquid water. Am. Mineral. 98, 897–906.

Hurowitz, J.A., Grotzinger, J.P., Fischer, W.W., McLennan, S.M., Milliken, R.E., Stein, N., Vasavada, A.R., Blake, D.F., Dehouck, E., Eigenbrode, J.L., Fairén, A.G., Frydenvang, J., Gellert, R., Grant, J.A., Gupta, S., Herkenhoff, K.E., Ming, D.W., Rampe, E.B., Schmidt, M.E., Siebach, K.L., Stack-Morgan, K., Sumner, D.Y., Wiens, R.C., 2017. Redox stratification of an ancient lake in Gale crater, Mars. Science 356.

Kounaves, S.P., Hecht, M.H., Kapit, J., Gospodinova, K., DeFlores, L., Quinn, R.C., Boynton, W.V., Clark, B.C., Catling, D.C., Hredzak, P., Ming, D.W., Moore, Q., Shusterman, J., Stroble, S., West, S.J., Young, S.M.M., 2010. Wet chemistry experiments on the 2007 Phoenix Mars Scout Lander mission: data analysis and results. J. Geophys. Res., Planets 115.

Lasaga, A., 1998. Kinetic Theory in the Earth Sciences. Princeton University Press, New Jersey.

Laudone, G.M., Gribble, C.M., Jones, K.L., Collier, H.J., Matthews, G.P., 2015. Validated a priori calculation of tortuosity in porous materials including sandstone and limestone. Chem. Eng. Sci. 131, 109–117.

Li, L., Maher, K., Navarre-Sitchler, A., Druhan, J., Meile, C., Lawrence, C., Moore, J., Perdrial, J., Sullivan, P., Thompson, A., Jin, L., Bolton, E.W., Brantley, S.L., Dietrich, W.E., Mayer, K.U., Steefel, C.I., Valocchi, A., Zachara, J., Kocar, B., McIntosh, J., Tutolo, B.M., Kumar, M., Sonnenthal, E., Bao, C., Beisman, J., 2017. Expanding the role of reactive transport models in critical zone processes. Earth-Sci. Rev. 165, 280–301.

Mackenzie, F.T., 2005. Sediments, Diagenesis and Sedimentary Rocks.

Maher, K., 2010. The dependence of chemical weathering rates on fluid residence time. Earth Planet. Sci. Lett. 294, 101–110.

Maher, K., Steefel, C.I., DePaolo, D.J., Viani, B.E., 2006. The mineral dissolution rate conundrum: insights from reactive transport modeling of U isotopes and pore fluid chemistry in marine sediments. Geochim. Cosmochim. Acta 70, 337–363.

Maher, K., Steefel, C.I., White, A.F., Stonestrom, D.A., 2009. The role of reaction affinity and secondary minerals in regulating chemical weathering rates at the Santa Cruz Soil Chronosequence, California. Geochim. Cosmochim. Acta 73, 2804–2831.

Martin, P.E., Farley, K.A., Baker, M.B., Malespin, C.A., Schwenzer, S.P., Cohen, B.A., Mahaffy, P.R., McAdam, A.C., Ming, D.W., Vasconcelos, P.M., Navarro-González, R., 2017. A two-step K–Ar experiment on Mars: dating the diagenetic formation of jarosite from Amazonian groundwaters. J. Geophys. Res., Planets 122, 2803–2818.

McAdam, A.C., Zolotov, M.Y., Mironenko, M.V., Sharp, T.G., 2008. Formation of silica by low-temperature acid alteration of Martian rocks: physical–chemical constraints. J. Geophys. Res. 113.

McLennan, S.M., Anderson, R.B., Bell, J.F., Bridges, J.C., Calef, F., Campbell, J.L., Clark, B.C., Clegg, S., Conrad, P., Cousin, A., Des Marais, D.J., Dromart, G., Dyar, M.D., Edgar, L.A., Ehlmann, B.L., Fabre, C., Forni, O., Gasnault, O., Gellert, R., Gordon, S., Grant, J.A., Grotzinger, J.P., Gupta, S., Herkenhoff, K.E., Hurowitz, J.A., King, P.L., Le Mouélic, S., Leshin, L.A., Léveillé, R., Lewis, K.W., Mangold, N., Maurice, S., Ming, D.W., Morris, R.V., Nachon, M., Newsom, H.E., Ollila, A.M., Perrett, G.M., Rice, M.S., Schmidt, M.E., Schwenzer, S.P., Stack, K., Stolper, E.M., Sumner, D.Y., Treiman, A.H., VanBommel, S., Vaniman, D.T., Vasavada, A., Wiens, R.C., Yingst, R.A., Team, M.S., 2014. Elemental geochemistry of sedimentary rocks at Yellowknife Bay, Gale crater, Mars. Science 343.

Nachon, M., Mangold, N., Forni, O., Kah, L.C., Cousin, A., Wiens, R.C., Anderson, R., Blaney, D., Blank, J.G., Calef, F., Clegg, S.M., Fabre, C., Fisk, M.R., Gasnault, O., Grotzinger, J.P., Kronyak, R., Lanza, N.L., Lasue, J., Deit, L.L., Mouélic, S.L., Maurice, S., Meslin, P.Y., Oehler, D.Z., Payré, V., Rapin, W., Schröder, S., Stack, K., Sumner, D., 2017. Chemistry of diagenetic features analyzed by ChemCam at Pahrump Hills, Gale crater, Mars. Icarus 281, 121–136.

Navarre-Sitchler, A., Steefel, C.I., Sak, P.B., Brantley, S.L., 2011. A reactive-transport model for weathering rind formation on basalt. Geochim. Cosmochim. Acta 75, 7644–7667.

Navarre-Sitchler, A., Steefel, C.I., Yang, L., Tomutsa, L., Brantley, S.L., 2009. Evolution of porosity and diffusivity associated with chemical weathering of a basalt clast. J. Geophys. Res. 114.

Pye, K., Tsoar, H., 2008. Aeolian Sand and Sand Dunes. Springer, Berlin.

Rampe, E.B., Ming, D.W., Blake, D.F., Bristow, T.F., Chipera, S.J., Grotzinger, J.P., Morris, R.V., Morrison, S.M., Vaniman, D.T., Yen, A.S., Achilles, C.N., Craig, P.I., Des Marais, D.J., Downs, R.T., Farmer, J.D., Fendrich, K.V., Gellert, R., Hazen, R.M., Kah, L.C., Morookian, J.M., Peretyazhko, T.S., Sarrazin, P., Treiman, A.H., Berger, J.A., Eigenbrode, J., Fairén, A.G., Forni, O., Gupta, S., Hurowitz, J.A., Lanza, N.L., Schmidt, M.E., Siebach, K., Sutter, B., Thompson, L.M., 2017. Mineralogy of an ancient lacustrine mudstone succession from the Murray formation, Gale crater, Mars. Earth Planet. Sci. Lett. 471, 172–185.

Schmidt, M.E., King, P.L., Gellert, R., Elliott, B., Thompson, L., Berger, J.A., Bridges, J.C., Campbell, J.L., Ehlmann, B.L., Grotzinger, J., Hurowitz, J.A., Leshin, L.A., Lewis, K.W., McLennan, S.M., Ming, D.W., Perrett, G., Pradler, I., Stolper, E.M., Squyres, S.W., Treiman, A.H., Team, M.S., 2013. APXS of first rocks encountered by curiosity in Gale crater: geochemical diversity and volatile element (K and Zn) enrichment. In: 44th Lunar and Planetary Science Conference. Lunar and Planetary Institute, Houston. Abstract #1278.

Stack, K.M., Grotzinger, J.P., Kah, L.C., Schmidt, M.E., Mangold, N., Edgett, K.S., Sumner, D.Y., Siebach, K.L., Nachon, M., Lee, R., Blaney, D.L., Deflores, L.P., Edgar, L.A., Fairén, A.G., Leshin, L.A., Maurice, S., Oehler, D.Z., Rice, M.S., Wiens, R.C., 2014. Diagenetic origin of nodules in the Sheepbed member, Yellowknife Bay formation, Gale crater, Mars. J. Geophys. Res., Planets 119, 2014JE004617.

Steefel, C.I., Appelo, C.A.J., Arora, B., Jacques, D., Kalbacher, T., Kolditz, O., Lagneau, V., Lichtner, P.C., Mayer, K.U., Meeussen, J.C.L., Molins, S., Moulton, D., Shao, H., Šimůnek, J., Spycher, N., Yabusaki, S.B., Yeh, G.T., 2015. Reactive transport codes for subsurface environmental simulation. Comput. Geosci. 19, 445–478.

Steefel, C.I., Lasaga, A.C., 1994. A coupled model for transport of multiple chemical species and kinetic precipitation/dissolution reactions with application to reactive flow in single phase hydrothermal systems. Am. J. Sci. 294, 529–592.

Steefel, C.I., MacQuarrie, K.T.B., 1996. Approaches to modeling of reactive transport in porous media. In: Lichtner, P.C., Steefel, C.I., Oelkers, E.H. (Eds.), Reactive Transport in Porous Media. Reviews in Mineralogy. Mineralogical Society of America, Chantilly, Virginia, pp. 83–129.

Sutter, B., McAdam, A.C., Mahaffy, P.R., Ming, D.W., Edgett, K.S., Rampe, E.B., Eigenbrode, J.L., Franz, H.B., Freissinet, C., Grotzinger, J.P., Steele, A., House, C.H., Archer, P.D., Malespin, C.A., Navarro-González, R., Stern, J.C., Bell, J.F., Calef, F.J., Gellert, R., Glavin, D.P., Thompson, L.M., Yen, A.S., 2017. Evolved gas analyses of sedimentary rocks and eolian sediment in Gale crater, Mars: results of the Curiosity rover's sample analysis at Mars instrument from Yellowknife Bay to the Namib Dune. J. Geophys. Res., Planets 122, 2574–2609.

Vaniman, D.T., Martínez, G.M., Rampe, E.B., Bristow, T.F., Blake, D.F., Yen, A.H., Ming, D.W., Rapin, W., Meslin, P.-Y., Morookian, J.M., Downs, R.T., Chipera, S.J., Morris, R.V., Morrison, S.M., Treiman, A.H., Achilles, C.N., Grotzinger, J.P., Hazen, R.M., Crisp, J.A., 2017. Calcium sulfates at Gale crater and limitations on gypsum stability. In: 48th Lunar and Planetary Science Conference. Lunar and Planetary Institute, Houston. Abstract #1661.

Velbel, M.A., 1993. Constancy of silicate-mineral weathering-rate ratios between natural and experimental weathering: implications for hydrologic control of differences in absolute rates. Chem. Geol. 105, 89–99.

Watkins, J.A., Grotzinger, J., Stein, N., Banham, S.G., Gupta, S., Rubin, D., Stack, K.M., Edgett, K.S., 2016. Paleotopography of erosional unconformity, base of Stimson formation, Gale crater, Mars. In: 47th Lunar and Planetary Science Conference. Lunar and Planetary Institute, Houston. Abstract #2939.

Wilson, A.M., Boles, J.R., Garven, G., 2000. Calcium mass transport and sandstone diagenesis during compaction-driven flow: Stevens Sandstone, San Joaquin basin, California. Geol. Soc. Am. Bull. 112, 845–856.

Wolff-Boenisch, D., Gislason, S.R., Oelkers, E.H., Putnis, C.V., 2004. The dissolution rates of natural glasses as a function of their composition at pH 4 and 10.6, and temperatures from 25 to 74 °C. Geochim. Cosmochim. Acta 68, 4843–4858.

Yen, A.S., Ming, D.W., Vaniman, D.T., Gellert, R., Blake, D.F., Morris, R.V., Morrison, S.M., Bristow, T.F., Chipera, S.J., Edgett, K.S., Treiman, A.H., Clark, B.C., Downs, R.T., Farmer, J.D., Grotzinger, J.P., Rampe, E.B., Schmidt, M.E., Sutter, B., Thompson, L.M., 2017. Multiple stages of aqueous alteration along fractures in mudstone and sandstone strata in Gale crater, Mars. Earth Planet. Sci. Lett. 471, 186–198.

Zolotov, M.Y., Mironenko, M.V., 2007. Timing of acid weathering on Mars: a kinetic–thermodynamic assessment. J. Geophys. Res. 112.